

Detection of Surface Discontinuities in Additively Manufactured AlSi10Mg Using Thermoelastic Stress Analysis

Joshua Rodrigues[*1, 2], Matthew Pelosi[3], Wayne Foster[3], Simon Barter[1] & Raj Das[1, 2]

[1]Department of Aerospace Engineering, RMIT University, Melbourne Australia
[2]Centre for Additive Manufacturing, RMIT University, Melbourne, Australia
[3]Platforms Division, Defence Science and Technology Group, Fishermans Bend, Australia

Abstract

Surface discontinuities, such as porosity and roughness, are a common occurrence in laser powder bed fusion (L-PBF) components and can affect the fatigue performance of load-bearing structures. Methods to assess and identify the surface-based discontinuities that could lead to fatigue life reduction are hence essential. Conventional methods using X-ray computed tomography and ultrasonic inspection are limited by setup complexity and surface characteristics. This work utilises thermoelastic stress analysis (TSA), an optical non-destructive evaluation (NDE) technique, to identify and assess surface discontinuities in lightweight L-PBF aluminium alloy, AlSi10Mg, test articles. An as-built tensile specimen was compared to one with flat-bottom holes (FBHs) introduced to represent discontinuities. Five hole depths and five hole diameters were assessed. Strain gauge calibrated TSA scans were compared to numerical finite element (FE) models to compare surface stresses. TSA could effectively detect the FBHs (introduced from one side) from both sides of the specimen , and the stress concentration effect agreed with the FE models. On the non-hole side, the sensitivity was lower than from the side where the holes were introduced. The FBHs up to 2.5 mm from the inspected surface could be identified when the holes were 3.0 mm or more in diameter. TSA, as a rapid stress raiser assessment method, appears to be a viable NDE technique that could aid the design and qualification of lightweight structures that include complex internal geometric features.

Keywords: thermoelastic stress analysis, surface discontinuities, L-PBF AlSi10Mg, finite element method, non-destructive evaluation

1. Introduction

Additive manufacturing (AM) is an evolving fabrication technique that creates structures by adding material to produce a near net shape component. Laser powder bed fusion (L-PBF) is a common type of powder-based AM method used to fabricate metallic components, being highly attractive for complex, critical, load-bearing aerospace applications [1]. The unique capabilities of L-PBF allow complete control over the shape, composition and functionality of designs that can be tailored for specific applications [2]. However, the L-PBF process can introduce several types of discontinuities during fabrication, which can lead to potential sites for failure initiation, particularly the development of fatigue cracks [3]. Such discontinuities include surface porosity, roughness and lack of fusion inclusions [4]. Despite their presence, in situ assessment can be difficult due to their size and unique morphological characteristics. This difficulty is further heightened for surfaces that are not visible from the outside of the part. This can include either after manufacture or, from a maintenance point of view, after the part has been mated to the main structure, such as within sealed bays [5]. Therefore, methods for non-destructive evaluation (NDE) to detect internal discontinuities from the external surfaces can be advantageous to structural health monitoring.

Conventional methods for discontinuity detection within aerospace structures include X-ray computed

tomography and ultrasonic inspection. However, these methods are often expensive and require robust machinery for high accuracy or have limitations for complex geometry. These methods also do not have the capability to produce strain (stress) maps to indicate the severity of discontinuities under applied mechanical loading. This is an important characteristic for load-bearing structures in critical aerospace applications that can allow the identification of damage, as well as verify the structural performance of the structure. Stress assessment is generally performed using numerical methods, such as finite element (FE) analysis. This provides additional challenges if poorly defined geometries are used. Thermoelastic stress analysis (TSA) provides the unique capability to directly identify and analyse structural discontinuities as an NDE technique. TSA is an established full-field, non-contact optical method for surface strain (stress) assessment. This relies on the thermoelastic effect, where a reversible temperature change is produced by elastic deformation within a structure [6]. For adiabatic conditions, the temperature change is proportional to the change in the sum of principal stresses. This is known as the bulk principal stress and governed by the relation in Equation 1 [7], in its simplest form.

$$\Delta T = -\frac{\alpha}{\rho C_p} T \Delta \sigma \quad (1)$$

Here, ΔT represents the change in temperature of the structure, $\Delta \sigma$ is the change in the first stress invariant, and T is the absolute temperature of the structure. The preceding term is material-specific, comprising of α, the linear coefficient of thermal expansion, ρ, the material density, and C_p, the specific heat at constant pressure. TSA has proven to be an effective NDE technique for the validation of aircraft structures [7], and for identifying stress 'hot spots' and progressive damage such as fatigue cracks [8]. More recently, TSA has been applied to give stress visualisation in geometrically complex L-PBF metallic structures, including aerospace components [9], biomimetic designs [10] and lattice structures [11], for their assessment. However, this approach has not been considered for the analysis of surfaces and subsurface-based discontinuities that are not directly visible from outside the structure during loading. Since heat can dissipate through the thickness of materials, internal stress distributions can also be detected from the outside. Therefore, TSA presents a method that can allow the detection of internal stress raisers from the outer surface.

This paper presents a method that can be used to detect internal discontinuities based on TSA from the external surface. Here, L-PBF tensile specimens were built and scanned with a microbolometer under cyclic loading conditions. A standard tensile specimen was compared to one with various representative surface discontinuities in the form of flat-bottom holes (FBHs) that were drilled from one side only. Five hole diameters and five hole depths were assessed from both sides of the specimen to evaluate the effectiveness of the TSA method. The temperature readings were converted to stresses with the aid of calibrated strain gauge rosettes within the scan area, and these results were compared to numerical FE simulations.

2. Materials and Methodology

2.1 Specimen Design and Test Setup

Tensile 'dog bone' specimens – a relatively conventional configuration for both subtractive and AM part investigations, with 3.0 mm thickness, were fabricated using L-PBF through an SLM 500HL machine. The low-density L-PBF aluminium alloy, AlSi10Mg, was used due to its ease of L-PBF manufacturing and because it has an efficient strength-to-weight ratio, is relatively affordable and is of high interest for aerospace applications [1]. The specimens were fabricated vertically upwards with a build layer thickness of 30 µm per pass. The laser power was 370 W, the laser scan speed was 1335 mm/s, and the hatch spacing was 170 µm. FBHs were milled into one face of the specimens, denoted as the back face. The opposite, clean surface is referred to here as the front face. Five hole diameters and five hole depths were created, resulting in 25 unique holes, as shown in Fig. 1a. The hole depths were from 0.5 mm to 2.5 mm in increments of 0.5 mm, enabling a step stress response for each discontinuity depth. These artificial features represented discontinuities that could be induced by damage or be intentional to the design.

Cyclic loading (a requirement for the TSA method) was performed in a 100 kN Instron servo-hydraulic uniaxial testing machine. A Gobi+ 640 Series GigE uncooled microbolometer (thermal imaging camera) was used to capture the thermal response of the test article. The Microbolometer Thermoelastic Evaluation software application (MiTE, version 1.3.0.0) was used to record, calibrate and analyse the TSA data. A constant amplitude, cyclic load was required for the TSA process, and the control signal from the machine was interfaced to the MiTE software. The TSA setup is presented

in Fig. 1b. A loading frequency of 5.0 Hz was applied for each test. The load applied was from 0.0 to 3.0 kN. A preliminary FE model was analysed to determine that this was an appropriate load to be applied. The specimen had to remain within its elastic regime to enable an effective TSA scan, so the applied load ensured that no part of the specimen experienced plastic yielding. The same load was applied to each specimen. The scanned surfaces were painted with a high-emissivity, low-reflectivity matte paint to reduce incident radiation reflections and improve the TSA scan quality.

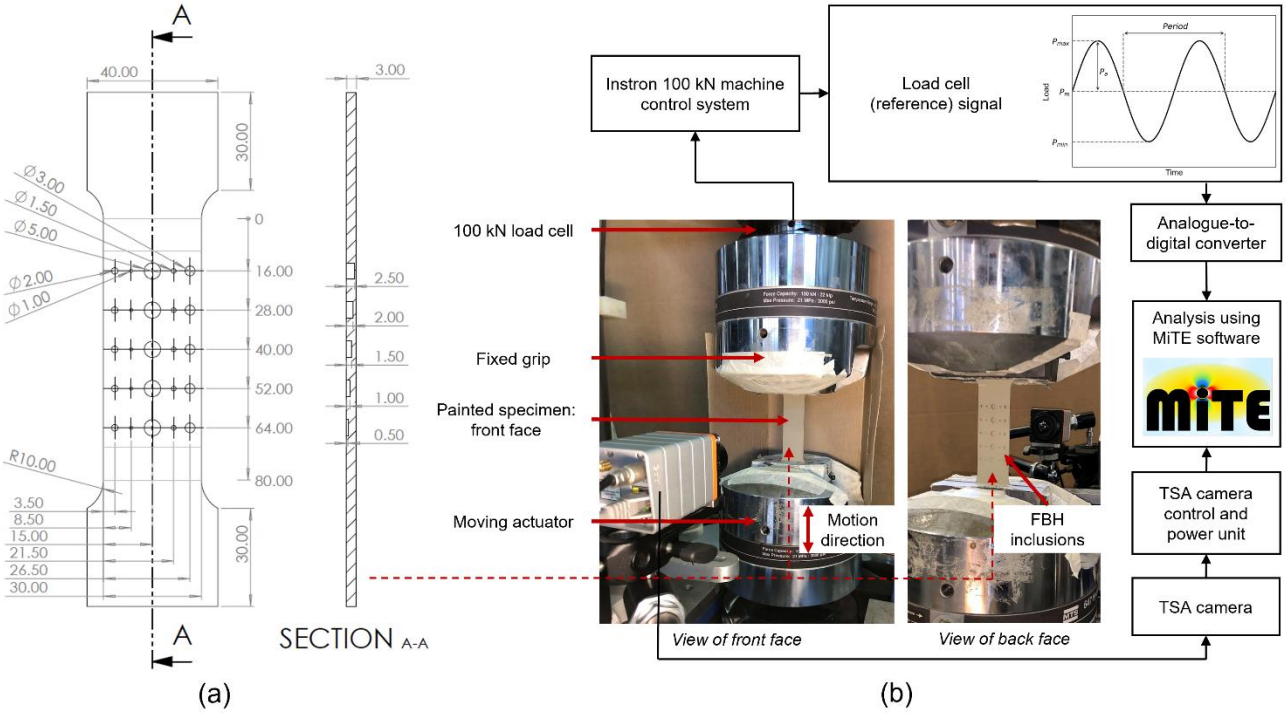


Figure 1 – The FBH specimen with (a) the layout of FBHs on the back face, and (b) the experimental test setup with the integrated TSA workflow.

2.2 Finite Element Modelling

FE modelling was performed using Abaqus CAE (version 2023) as a method of validation for the experimental TSA scans. Fig. 2a presents the representative loading and boundary conditions applied to mimic the experimental test setup. A strain gauge rosette was affixed to the specimen, at the location and with the orientation shown in Fig. 2b. The raw TSA scans were captured as temperature maps in nominal degrees kelvin. To convert the temperature to strain and obtain a quantitative strain field, independent strain measurements in the field of view were required. To this end, the three-gauge rosette was applied to the specimens after the TSA scanning process in a region that was assessed to have a uniform stress field (from the FE results). The first stress invariant could then be derived using the material properties and application of Hooke's law.

Solid hexahedral linear elements (notation C3D8 in Abaqus) with linear-elastic material behaviour were used, as shown in Fig. 2c. A mesh convergence study was performed on each model to ensure suitable computational accuracy with appropriate simulation time. A fine mesh was applied around the FBHs for higher accuracy. The selected mesh for the bulk specimen had a seed size of 0.2 mm in the gauge section and 129,208 elements. The FBH specimen had a seed size of 0.205 mm in the gauge region and a total number of 547,121 elements. The material properties were obtained through tensile testing of the L-PBF AlSi10Mg alloy according to the ASTM E8 standard. The Young's modulus was found to be 58.27 ± 0.71 MPa, and a Poisson's ratio of 0.3 was used.

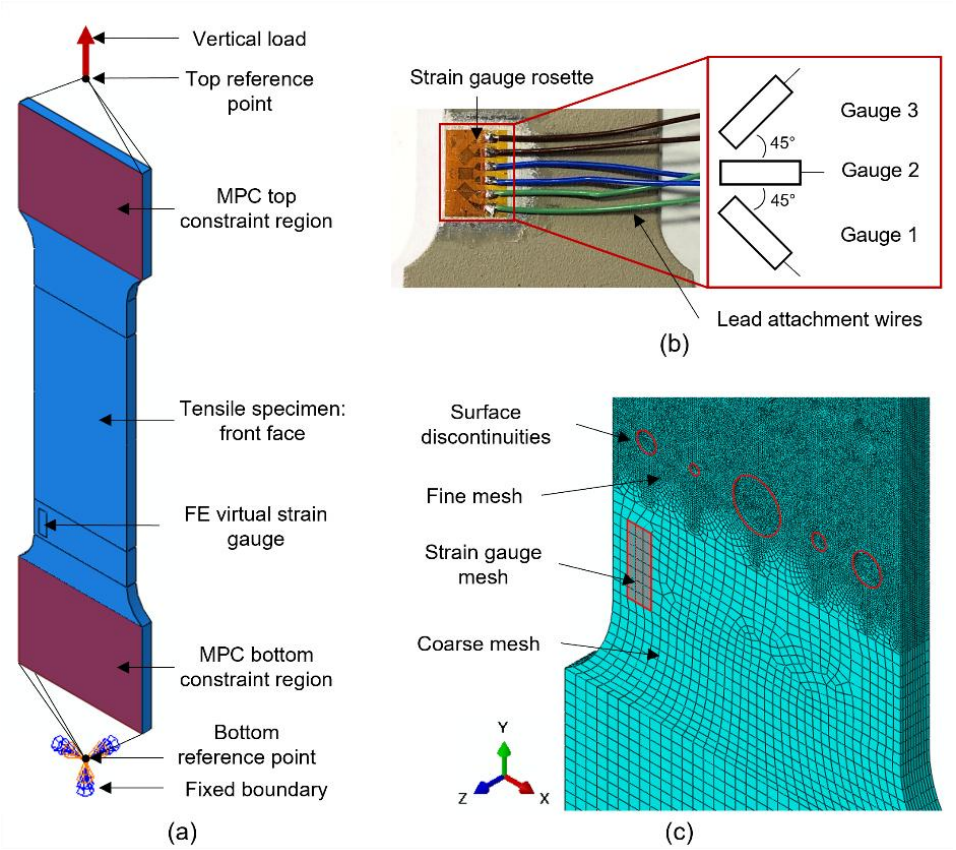


Figure 2 – Numerical approach for tensile specimens, including (a) the representative loading and boundary conditions in the FE model, (b) the strain gauge rosette location, and (c) the converged FE mesh for the specimens with FBHs.

3. Results and Discussion

The quantitative stress distribution, as well as the effect of the hole diameters and depths, was compared against a standard tensile specimen of the same configuration (without holes). The quantitative TSA stress scans were also compared against the FE simulations to verify the findings. Previously, Rajic *et al.* [12] studied the interaction of a composite skin with an internal core structure based on the TSA surface stress measurements. The present investigation aimed to extend upon this concept and use TSA to identify internal discontinuities from an external surface.

3.1 Quantitative stress comparison

The bulk tensile specimen was first analysed to use as a baseline comparison against the FBH specimen. The strain gauge data was collected following the scanning process to enable a quantitative calibration of the scans. All experimental TSA scan results had good agreement with the FE models, being within ~6% at the gauge location.

Fig. 3 presents the first stress invariant profiles of each scanned face using TSA and the corresponding FE result. The bulk specimen, Fig. 3a, had a mostly uniform stress distribution throughout the gauge section. Minor stress peaks were present towards the grip section due to the load transfer from the grips and the radii between the grip sections and the gauge length. The scans of the FBH specimen, however, showed much more stress variability and signified the influence of the FBHs. On the back face (Fig. 3b), where the holes were milled, the FBHs were obvious, as were the locations of high stress concentration associated with these holes. This resulted in an asymmetric stress distribution on the surface of the specimen. On the front face (Fig. 3c), where the FBHs could not directly be seen, the resultant changes in the stress field could still be identified. This appeared most noticeable at the locations with the greatest hole depth, meaning the thinnest walls, and decreased with decreasing hole depth.

The corresponding FE results showed agreement with the TSA scans around the FBHs on both faces. However, it was found that the FE results had higher peak stress values than the TSA results, particularly around the locations perpendicular to the loading direction. This was primarily due to the

TSA camera not being focused on these individual regions, resulting in the detector's pixel resolution being low at those regions and hence the low fidelity of the results in these regions.

In addition, the present approach did not consider the effect of mean stress during the scanning process. The mean stress effect considers the variations in mechanical performance due to the change in Young's modulus and Poisson's ratio with temperature during cyclic loading. This can produce discrepancies in regions of high-stress concentrations [13], and inhibit the effectiveness of the TSA approach for metals susceptible to this effect, such as titanium. However, this paper utilises aluminium, which has a higher thermal conductivity, and reduces the mean stress effect. Additionally, verifying the peak stresses in the structure was not the focus of this investigation. Rather, it was focused on identifying those regions with stress peaks and, in general, the distribution of stresses. Hence, excluding the mean stress effect did not greatly affect the resultant findings and was still appropriate to identify the FBHs in the specimen.

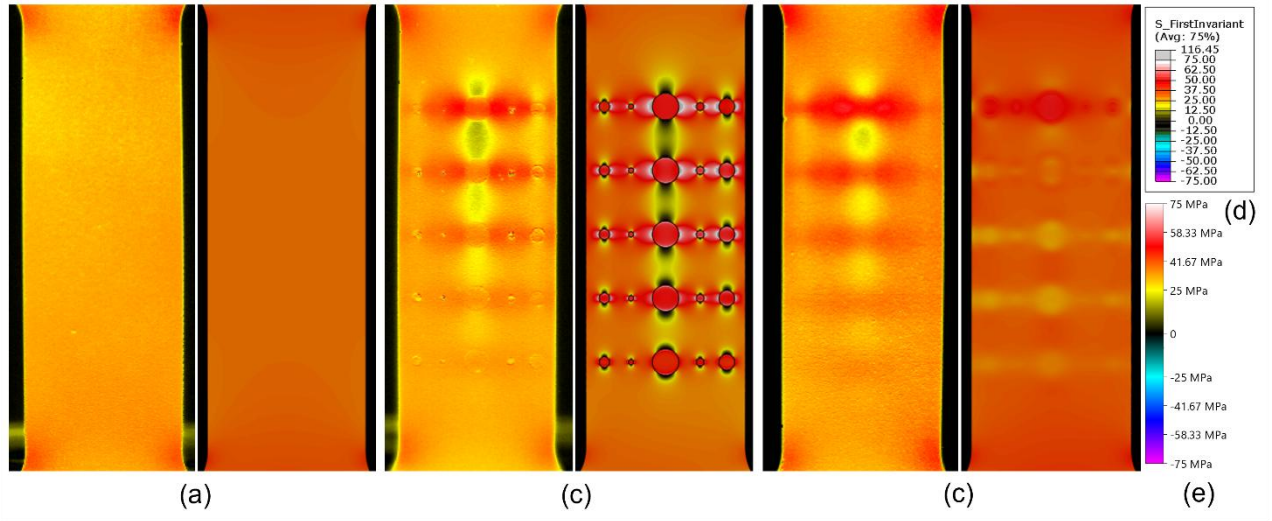


Figure 3 – Quantitative thermoelastic stress comparison of the specimen faces between (left) the TSA scan and (right) the FE results for (a) the bulk specimen and the FBH specimen (b) back face, and (c) front face. The corresponding stress legend scales are presented for (d) the FE results and (e) the TSA scan results.

3.2 Effect of Hole Diameter and Depth

Path analyses of the stresses were performed on both faces of the FBHs to investigate the influence of hole diameter and depth. Fig. 4 shows the analysis of hole FBHs on the back face of the specimen, considering hole diameter. A distinct path was drawn for each hole depth across the diameter of each hole, Fig. 4a, and the stresses are plotted in Fig. 4b. The FBHs could be identified for each depth through a reduction in stress along the diameter of the hole, which is indicated by the shaded bars on the Fig. 4b plot. For each diameter, the deepest holes (2.5 mm) were most effectively observed, and became less definitive with reducing hole depth. This was due to the difference in stress between the specimen face and the milled surface of the FBH. The locations of stress reduction aligned with the indicated locations of the discontinuity diameters along each of the paths examined.

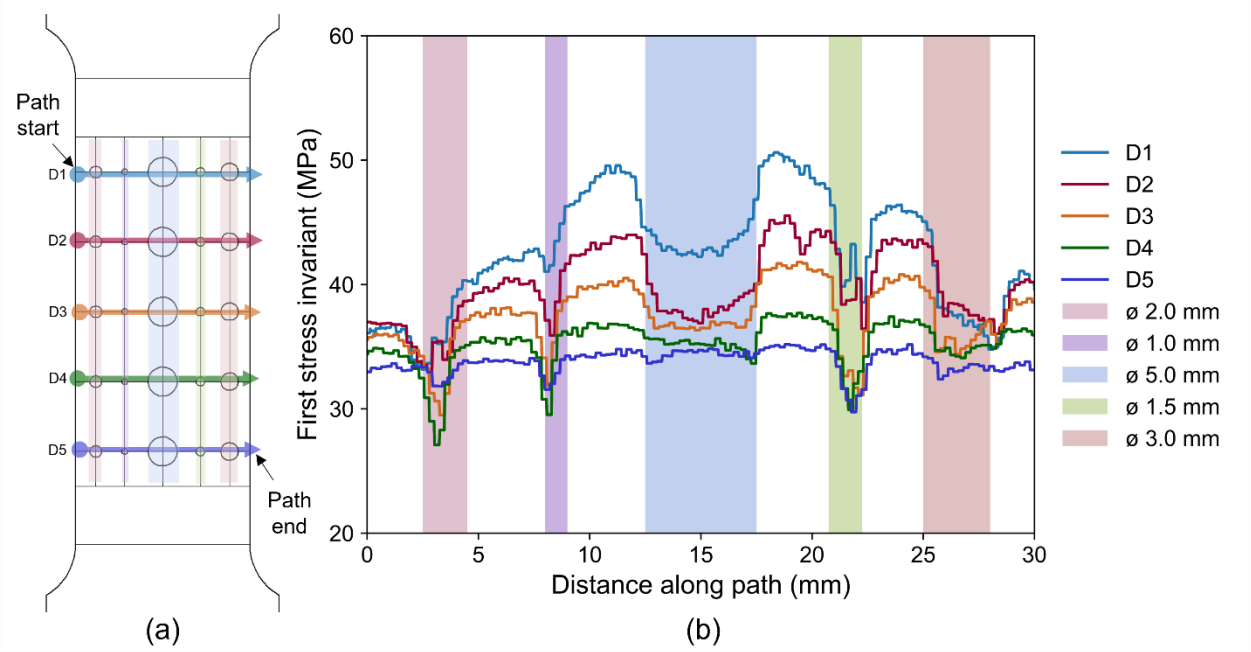


Figure 4 – Quantitative path analysis on the FBH specimen back face concerning hole diameter, including (a) the defined paths, and (b) the corresponding stress along each path.

From the front face, the results, using the same analysis paths, are presented in Fig. 5. Note that the locations of the holes are reversed around the longitudinal axis due to viewing them from the front face. Fig. 5b shows the change in stress along the FBH paths as before on the front face. The influence of the FBHs was less apparent than from the back face. The deeper holes of 2.5 mm, 2.0 mm and 1.5 mm showed the greatest change in stress, particularly for the larger hole diameters of 5.0 mm and 3.0 mm. This was due to there being a large change in material thickness presenting an identifiable stress step between the specimen surface and hole surface from the FBH inclusion. Hole depths less than 1.5 mm, and diameters smaller than 3.0 mm, were found difficult to effectively identify. This was due to the low temperature change, resulting from the low stress change, between the bulk material and the remaining material with the FBH.

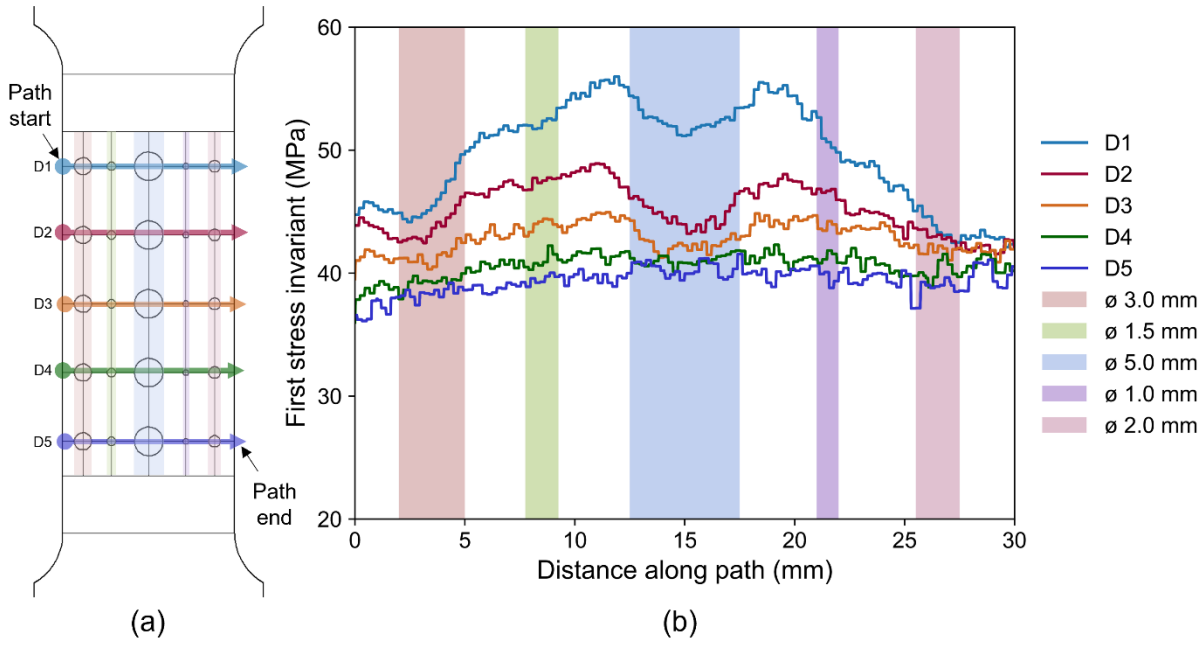


Figure 5 – Quantitative path analysis on the FBH specimen front face concerning hole diameter, including (a) the defined paths, and (b) the corresponding stress along each path.

3.3 TSA-FE Comparison

A quantitative comparison between the TSA and FE results was also investigated to assess the accuracy of the TSA process. This was performed on the front face of the specimen at the centroid of the FBH locations. The two largest hole diameters (3.0 mm and 5.0 mm) and three hole depths (2.5 mm, 2.0 mm, and 1.5 mm) were assessed, with the results presented in Table 1. It was found that the TSA scans had good agreement with the FE results for the deepest hole, with both hole diameters having less than 3.5% error in stress. However, the relative error increased with decreasing hole depth. This was attributed to the fidelity of the TSA scan with the low loads applied and increased diffusion throughout the sections with increased thickness (lower hole depth). This analysis identified the accuracy of the TSA approach for various hole depths and diameters, compared to FE results, to quantitatively identify the effect of discontinuities from an untouched face.

Table 1 – Comparison between the TSA and FE first stress invariant results in the centroid of the FBHs from the front face.

	Hole diameter					
	3.0 mm			**5.0 mm**		
Hole depth	**TSA (MPa)**	**FE (MPa)**	**Error (%)**	**TSA (MPa)**	**FE (MPa)**	**Error (%)**
2.5 mm	45.55 ± 0.90	46.00	0.99	51.80 ± 0.40	50.06	3.36
2.0 mm	43.40 ± 0.66	34.06	21.52	44.05 ± 0.53	35.31	19.84
1.5 mm	41.05 ± 0.51	30.57	25.54	41.95 ± 0.43	29.43	29.84

4. Conclusions

This investigation utilised TSA to detect surface discontinuities in the form of various FBHs in L-PBF AlSi10Mg specimens from the side where the discontinuities were introduced and the side where they were not visible. Quantitative experimental TSA scans were compared to FE modelling results. The effects of hole depth and diameter were both investigated. It was found that TSA could effectively identify and assess the FBHs based on the stress distribution on both the hole entry side and the clean, opposing side. The TSA approach could identify all FBHs from the entry side. From the opposing surface, however, there were limitations, where the FBHs required diameters of 3.0 mm or greater, and depths of 1.5 mm or greater, to be effectively identified. From an identifiable stress level perspective, the comparison of these scans to FE results showed a clear trend. This approach was most accurate for holes with a greater identifiable step in stresses compared to the bulk stress of the specimen. The findings show that TSA is a viable method to quantitatively and qualitatively assess surface-based, and to some extent embedded, discontinuities for L-PBF AlSi10Mg structures. This approach can be applied to applications such as the design verification and analysis of lightweight aerospace structures that include complex geometric features in both conventional and L-PBF built parts.

5. Contact Author Email Address

The contact author's email address for this work is: joshua.rodrigues@student.rmit.edu.au

6. Copyright Statement

The authors confirm that they, and/or their company or organization, hold copyright on all of the original material included in this paper. The authors also confirm that they have obtained permission, from the copyright holder of any third party material included in this paper, to publish it as part of their paper. The authors confirm that they give permission, or have obtained permission from the copyright holder of this paper, for the publication and distribution of this paper as part of the ICAS proceedings or as individual off-prints from the proceedings.

References

[1] Blakey-Milner, B., Gradl, P., Snedden, G., Brooks, M., Pitot, J., Lopez, E., Leary, M., Berto, F., and du Plessis, A., 2021, Metal additive manufacturing in aerospace: A review, *Materials & Design,* vol. 209, pp. 110008.

[2] Huang, Y., Leu, M.C., Mazumder, J., and Donmez, A., 2015, Additive manufacturing: current State, future potential, gaps and needs, and recommendations, *Journal of Manufacturing Science and Engineering,* vol. 137 (1).

[3] Sanaei, N., and Fatemi, A., 2021, Defects in additive manufactured metals and their effect on fatigue performance: A state-of-the-art review, *Progress in Materials Science,* vol. 117.

[4] Rogers, J., Elambasseril, J., Wallbrink, C., Krieg, B., Qian, M., Brandt, M., and Leary, M., 2024, The impact of surface orientation on surface roughness and fatigue life of laser-based powder bed fusion Ti-6Al-4V, *Additive Manufacturing,* vol. 85.

[5] Towsyfyan, H., Biguri, A., Boardman, R., and Blumensath, T., 2020, Successes and challenges in non-destructive testing of aircraft composite structures, *Chinese Journal of Aeronautics,* vol. 33 (3), pp. 771-791.

[6] Rajic, N., and Rowlands, D., 2013, Thermoelastic stress analysis with a compact low-cost microbolometer system, *Quantitative InfraRed Thermography Journal,* vol. 10 (2), pp. 135-158.

[7] Rajic, N., McSwiggen, D., McDonald, M., and Whiteley, D., 2018, In situ thermoelastic stress analysis – an improved approach to airframe structural model validation, *Quantitative InfraRed Thermography Journal,* vol. 16 (1), pp. 8-34.

[8] Brooks, C., and Rajic, N., 2022, Automated visual tracking of crack growth in coupon and component level fatigue testing using thermoelastic stress analysis, *International Journal of Fatigue,* vol. 163.

[9] Mukhaimar, A., Tennakoon, R., Rajic, N., Zambetta, F., Marzocca, P., Hoseinnezhad, R., Brooks, C., Van Der Velden, S., and Khauv, K., 2023, Stress visualization in geometrically complex structures using Thermoelastic Stress Analysis and Augmented Reality, *29th ACM Symposium on Virtual Reality Software and Technology,* pp. 1-2.

[10] Rodrigues, J., Das, R., Barter, S., Pelosi, M., and Foster, W., 2025, Methodology for the thermoelastic stress analysis of complex biomimetic structures: An alligator mandible case study, *European Journal of Mechanics - A/Solids,* vol. 109.

[11] Rodrigues, J., Pelosi, M., Foster, W., Barter, S., and Das, R., 2026, Assessment of strut discontinuities in additively manufactured lattice structures using thermoelastic stress analysis, *NDT & E International,* vol. 158.

[12] Rajic, N., Brooks, C., Wang, J., Forrester, C., and Swanton, G., 2017, Thermoelastic stress analysis for structural performance assessment of aerospace composites, In *21st International Conference on Composite Materials,* 20-25th August 2017*,* in Xi'an, China.

[13] Palumbo, D., and De Finis, R., 2023, Thermoelastic stress analysis in the presence of biaxial stresses in titanium: Effect of the mean stress on errors in stress evaluation, *Experimental Mechanics,* vol. 63 (8), pp. 1335-1351.